

THE THREE HUNDRED: $M_{\text{sub}} - V_{\text{circ}}$ relation

Atulit Srivastava,^{1,2}★ Weiguang Cui,^{1,2,3}† Massimo Meneghetti,^{4,5} Romeel Dave,^{3,5} Alexander Knebe,^{1,2,6} Antonio Ragagnin,^{7,8,9} Carlo Giocoli,^{4,5} Francesco Calura,⁴ Giulia Despali,^{7,10} Lauro Moscardini^{4,5,7} and Gustavo Yepes^{1,2}

¹Departamento de Física Teórica, M-8, Universidad Autónoma de Madrid, Cantoblanco 28049, Madrid, Spain

²Centro de Investigación Avanzada en Física Fundamental (CIAFF), Universidad Autónoma de Madrid, Cantoblanco, 28049 Madrid, Spain

³Institute for Astronomy, University of Edinburgh, Royal Observatory, Edinburgh EH9 3HJ, United Kingdom

⁴INAF-Osservatorio di Astrofisica e Scienza dello Spazio di Bologna, Via Piero Gobetti 93/3, 401 29 Bologna, Italy

⁵INFN-Sezione di Bologna, Viale Berti Pichat 6/2, 401 27, Bologna, Italy

⁶International Centre for Radio Astronomy Research, University of Western Australia, 35 Stirling Highway, Crawley, Western Australia 6009, Australia

⁷Dipartimento di Fisica e Astronomia "Augusto Righi", Alma Mater Studiorum Università di Bologna, via Gobetti 93/2, I-40129 Bologna, Italy

⁸INAF-Osservatorio Astronomico di Trieste, via G. B. Tiepolo 11, I-34143 Trieste, Italy

⁹IFPU – Institute for Fundamental Physics of the Universe, Via Beirut 2, I-34014 Trieste, Italy

¹⁰Institut für Theoretische Astrophysik, Zentrum für Astronomie, Heidelberg Universität, Albert-Ueberle-Str. 2, 69120, Heidelberg, Germany

Accepted XXX. Received YYY; in original form ZZZ

ABSTRACT

In this study, we investigate a recent finding based on strong lensing observations, which suggests that the sub-halos observed in clusters exhibit greater compactness compared to those predicted by Λ CDM simulations. To address this discrepancy, we performed a comparative analysis by comparing the cumulative mass function of sub-halos and the $M_{\text{sub}}-V_{\text{circ}}$ relation between observed clusters and 324 simulated clusters from THE THREE HUNDRED project, focusing on re-simulations using GADGET-X and GIZMO-SIMBA baryonic models. The sub-halos' cumulative mass function of the GIZMO-SIMBA simulated clusters agrees with observations, while the GADGET-X simulations exhibit discrepancies in the lower sub-halo mass range possibly due to its strong SuperNova feedback. Both GADGET-X and GIZMO-SIMBA simulations demonstrate a redshift evolution of the sub-halo mass function and the V_{max} function, with slightly fewer sub-halos observed at lower redshifts. Neither the GADGET-X nor GIZMO-SIMBA (albeit a little closer) simulated clusters' predictions for the $M_{\text{sub}}-V_{\text{circ}}$ relation align with the observational result. Further investigations on the correlation between sub-halo/halo properties and the discrepancy in the $M_{\text{sub}}-V_{\text{circ}}$ relation reveals that the sub-halo's half mass radius and galaxy stellar age, the baryon fraction and sub-halo distance from the cluster's centre, as well as the halo relaxation state play important roles on this relation. Nevertheless, we think it is still challenging in accurately reproducing the observed $M_{\text{sub}}-V_{\text{circ}}$ relation in our current hydrodynamic cluster simulation under the standard Λ CDM cosmology.

Key words:

gravitational lensing – galaxy clusters – galaxies – dark matter

1 INTRODUCTION

Cold dark matter (CDM) plays an essential role in the formation and evolution of galaxies and galaxy clusters. It can be detected solely through its gravitational effects, such as the bending of the light from background galaxies. Galaxy clusters are gravitationally bounded systems with a mass around 10^{14} to 10^{15} solar masses, and dark matter makes up approximately 80 per cent of their mass. Gravity drives the process of structure formation, with haloes assembling hierarchically over time. Galaxy cluster haloes, in particular, are among the late-forming structures (White & Frenk 1991; Tormen 1998; Giocoli et al. 2007). Inside galaxy clusters, hundreds to thousands of sub-halos are resident in local minimum potential (Springel

et al. 2001; Giocoli et al. 2010). These inner structures are known as sub-halos. Investigating and understanding these sub-halos will help us to understand galaxy cluster formation in detail.

The paper from Meneghetti et al. (2020) (hereafter M20) studied the gravitational lensing properties of both the cluster halos and sub-halos of the cluster samples observed in the Cluster Lensing and Supernova Survey with Hubble (CLASH Postman et al. 2012) and Hubble Frontier Fields (Lotz et al. 2017) and compared them to hydro-simulated galaxy clusters. In their study, M20 discovered that the Galaxy-Galaxy Strong Lensing (GGSL) probability from simulation, reconstructed means of lensing tool of Bergamini et al. (2019), is significantly lower compared to the observed clusters. This finding indicates that the observed clusters have much higher GGSL probability than those from hydrodynamic simulations under the Λ CDM cosmology. To support their argument, M20 used the maximum cir-

★ E-mail: ATULIT.SRIVASTAV@ESTUDIANTE.UAM.ES

† E-mail: weiguang.cui@uam.es; Talento-CM fellow

cular velocities, V_{circ}^1 , of sub-halos within galaxy clusters as a metric to assess the degree of compactness, as it directly reflects the sub-halo potential for producing the strong lensing events. This V_{circ} is associated with the 1D-velocity dispersion σ_0 by $V_{\text{circ}} = \sqrt{2}\sigma_0$, which is selected as one of the parameters in the lens modelling analysis of M20. They noticed that the sub-halos in observed clusters have higher V_{circ} values when compared to sub-halo samples from mass-matched clusters in the cosmological hydrodynamic simulations by Planelles et al. (2014). These findings suggest that the galaxies in these observed clusters are more efficient in lensing background sources and potentially more concentrated. The discrepancy between simulation and observation results may arise from limitations in the simulation's resolution or the presence of systematics. It has been suggested that the simulation output is sensitive to mass resolution and tidal disruption (van den Bosch et al. 2018; Green et al. 2021), which could potentially impact sub-halos properties. However, Meneghetti et al. (2022) (see also Ragagnin et al. 2022) found that the resolution does not affect the GGSL probability, which, however, seems sensitive to the galaxy formation model implemented in the simulations. Nevertheless, it is still difficult to simultaneously reproduce galaxies' stellar mass function and internal structure. Another possible explanation is that this issue arises from an inaccurate understanding of the nature of dark matter within the Λ CDM paradigm, which may necessitate the exploration of alternative models such as self-interacting dark matter (SIDM) models (Yang & Yu 2021; Bhattacharyya et al. 2022) and cold and sterile neutrino (SN) dark matter models (Despali et al. 2020).

Using the simulated galaxy clusters from the Hydrangea/C-EAGLE cosmological hydrodynamic simulations, Bahé (2021) did a similar comparison to the observed clusters, as in M20. Only one simulated cluster from Hydrangea at redshift $z = 0.4$ matches closely with the mass range of the observed sample presented in M20, with mass of $M_{200c}^2 > 5 \times 10^{14} h^{-1} M_{\odot}$. They claimed that sub-halos in this highly resolved simulation match well with the observations (see also another study by Robertson 2021 for resolution impact on simulation generated lensing signal). In their study, Bahé (2021) determined that V_{circ} is higher by a factor of 2 in Hydrangea and is consistent with respect to the observation trend. This increase in the offset of the maximum circular velocity was attributed to the inclusion of baryons in the simulations. The comparison made by Bahé (2021) between simulations with and without baryonic matter (i.e. dark matter only) revealed that sub-halos with a higher fraction of baryonic matter exhibited higher V_{circ} , implying that dense stellar cores capable of sustaining tidal stripping play a major role in explaining the observed high lensing signals (Armitage et al. 2019, also see Bahé et al. 2019; Joshi et al. 2019). Additionally, Bahé (2021) also checked the result from the Illustris-TNG300 simulation (Marinacci et al. (2018); Naiman et al. (2018); Nelson et al. (2019); Pillepich et al. (2018); Springel et al. (2018)), and argued that both Illustris-TNG300 and Hydrangea simulations predicted high V_{circ} values for massive sub-halos located in the vicinity of the cluster centre. Thus, Bahé (2021) concluded that there is no evidence of a significant disagreement between the observed sub-halos concentrations and predictions from the CDM model.

On the contrary, Ragagnin et al. (2022) examined the effect of

various numerical setups (such as resolution and softening length) and AGN feedback scheme on the interior structure of cluster sub-halos using six simulated zoomed-in regions of Dianoga, and they found contrasted results with respect to Bahé (2021). Their results suggested that regardless of the numerical configuration used, the sub-halos of simulated clusters were unable to reproduce the observed $M_{\text{sub}} - V_{\text{circ}}$ (M_{sub} , sub-halo mass) relation from Bergamini et al. (2019). This failure to reproduce the scaling relation was particularly evident for sub-halo masses $M_{\text{sub}} < 10^{11} h^{-1} M_{\odot}$, which corresponds to the mass range of interest for galaxy-galaxy strong lensing (GGSL) events. The simulated sub-halos exhibited V_{circ} values are approximately 30% smaller compared to the observed scaling relation presented by Bergamini et al. (2019). This was also observed for Hydrangea simulations discussed in Bahé (2021). The scaling relationship between M_{sub} (mass of sub-halos) and V_{circ} (circular velocity), as derived from simulations, shows good agreement with observations in the high mass range ($M_{\text{sub}} > 4 \times 10^{11} h^{-1} M_{\odot}$). However, concerns have been raised by Ragagnin et al. (2022) regarding the simulations' tendency to produce high stellar masses for sub-halos within this mass range. This discrepancy in stellar mass could potentially be a key factor contributing to the observed agreement in the $M_{\text{sub}} - V_{\text{circ}}$ relation for the high mass range, and it may be associated also with the Hydrangea simulations examined by Bahé (2021). Although the simulations can reproduce the correct scaling relationship between M_{sub} and V_{circ} by adjusting the AGN feedback strength, the resulting galaxies exhibit unrealistic properties, such as having larger stellar masses compared to observed galaxies. As demonstrated by Ragone-Figueroa et al. (2018), both Hydrangea and IllustrisTNG simulations show excessively large stellar masses in the brightest cluster galaxies. Therefore, it is important to emphasize that both Meneghetti et al. (2022) and Ragagnin et al. (2022) clearly stated that simulations are unable to simultaneously reconcile with the observed $M_{\text{sub}} - V_{\text{circ}}$ relationship in the two sub-halo mass regimes.

We would like to point out that all these previous studies are limited by the number of cluster samples which can not draw statistically solid conclusions as well as no correlation studies. In a recent letter, Meneghetti et al. (in prep.), performed a ray-tracing analysis of 324 galaxy clusters from the THE THREE HUNDRED³ and found that the GIZMO-SIMBA version run developed denser stellar cores and boosted the galaxy-galaxy strong lensing probability by a factor of ~ 3 than its GADGET-X counterparts. In this companion paper, we also use the simulated galaxy clusters from the THE THREE HUNDRED project, as detailed in Cui et al. (2018, 2022), to compare with the observed $M_{\text{sub}} - V_{\text{circ}}$ relation reported in M20. Although our simulated clusters have a slightly lower mass resolution than Planelles et al. (2014) and about 100 times lower than the Hydrangea simulated clusters, they have a significant advantage in terms of a large sample size, a relatively wide extensive mass range and, importantly, two different baryon models. Our sample includes approximately 10 times more simulated clusters than the Hydrangea sample used in Bahé (2021), and roughly 15 times more than the Dianoga simulation used in Ragagnin et al. (2022). These advantages allow us to statistically investigate and understand the discrepancy.

The paper is structured as follows: In Section 2, we provide an introduction to the THE THREE HUNDRED galaxy cluster simulation with the Amiga Halo Finder (AHF) halo catalogue which was used to identify host-halos and their corresponding sub-halos. We will also explain our methodology for selecting the samples of host halos

¹ We will use V_{circ} to denote the maximum circular velocities throughout this paper.

² M_{200c} represents the mass within a radius denoted as R_{200c} , measured from the center of a galaxy cluster's potential, where this radius signifies the region with an average density that is 200 times the critical density of the Universe.

³ <https://www.the300-project.org>

and their sub-halos. In Section 3, we compare the sub-halos mass distribution of M20 to three reference clusters with the predictions from the simulation and examine how it evolves with redshift. In Section 4, we present the cumulative sub-halo V_{circ} function for the simulations. In Section 5, we compare the observed M_{sub} and V_{circ} relation reported in Bergamini et al. (2019) with the one generated from the data set of simulated clusters in the THE THREE HUNDRED project. We also examine the influence of sub-halo and host-halo properties on the $M_{\text{sub}} - V_{\text{circ}}$ relationship. Finally, in Section 6 we will summarise our results.

2 SIMULATIONS

The THE THREE HUNDRED project, introduced in Cui et al. (2018), consists of an ensemble of 324 galaxy clusters that were modelled based on the extraction of a mass-complete sample with largest virial halo mass $M_{\text{vir}} \gtrsim 8 \times 10^{14} h^{-1} M_{\odot}$ at $z = 0$ from the Dark Matter-only Multidark simulation (MDPL2, Klypin et al. 2016). The MDPL2 simulation employs periodic boundary conditions with a cubic side of $1 \text{ Gpc}/h$ and contains 3840^3 dark matter particles, with a mass of $1.5 \times 10^9 h^{-1} M_{\odot}$. This dark matter-only simulation adopts cosmological parameters ($\Omega_M = 0.307$, $\Omega_B = 0.048$, $\Omega_{\Lambda} = 0.693$, $h = 0.678$, $\sigma_8 = 0.823$, $n_s = 0.96$) based on the Planck observations from Planck Collaboration et al. (2016). Each selected cluster is placed at the centre of the re-simulated box inside a high-resolution spherical region with a radius of $15 h^{-1} \text{ Mpc}$. The regions are filled with gas and dark matter particles (with $m_{\text{DM}} = 1.27 \times 10^9 h^{-1} M_{\odot}$ and $m_{\text{gas}} = 2.36 \times 10^8 h^{-1} M_{\odot}$) based on the original dark matter distribution, in accordance to the cosmological baryon fraction $\Omega_B = 0.048$. Beyond the $15 h^{-1} \text{ Mpc}$ range, the outer region is populated with low-resolution mass particles to simulate any large-scale tidal effects similar in a computationally efficient way compared to the original MDPL2 simulation. Subsequently, the 324 selected regions undergo re-simulation using different baryonic models and codes, namely GADGET-X (Rasia et al. 2015) and GIZMO-SIMBA (Davé et al. 2019; Cui et al. 2022). For each simulated cluster in the THE THREE HUNDRED project using GADGET-X and GIZMO-SIMBA, we have 128 snapshot files corresponding to redshifts ranging from $z = 17$ to 0.

The details regarding the GADGET-X and GIZMO-SIMBA codes used for the re-simulation of clusters are as follows:

- **GADGET-X:** It is an updated, modified version of GADGET3 code (Murante et al. 2010; Rasia et al. 2015; Planelles et al. 2017) in which the evolution of dark matter is followed by the gravity solver of the GADGET3 Tree-PM code, an updated version of GADGET2 code (Springel 2005). It incorporates an improved SPH scheme (Beck et al. 2016) with artificial thermal diffusion, time-dependent artificial viscosity, high-order Wendland C4 interpolating kernel, and wake-up scheme. The technique described in Wiersma et al. (2009) is used to compute gas cooling for an optically thin gas with consideration of the contribution of metals. Additionally, a uniform ultraviolet (UV) background is incorporated by adopting the approach outlined in Haardt & Madau (1995). Star formation in this work follows the approach described in Tornatore et al. (2007) and adopts the star formation algorithm presented by Springel & Hernquist (2003). This algorithm treats gas particles as multiphase, contributing to a self-regulating interstellar medium when their densities rise over a particular threshold. The star formation rate is determined solely by the gas density in this model. Stellar feedback, specifically supernova feedback, is implemented as a kinetic energy-driven scheme, following the prescription in Springel & Hernquist (2003). Each star particle

is treated as a single stellar population (SSP), and the evolution of each SSP is modelled following Chabrier (2003) stellar evolution prescriptions. Metals from Type Ia and Type II supernovae, as well as from asymptotic giant branch phases, are taken into account in the simulation, with the code following the evolution of 16 chemical species. The growth of black holes and the implementation of AGN feedback in GADGET-X are based on the refined model presented in Steinborn et al. (2015). In this model, super-massive black holes grow via Eddington-limited Bondi-Hoyle-like gas accretion, with a distinction made between hot and cold components.

- **GIZMO-SIMBA** It is based on the GIZMO cosmological hydrodynamical code (Hopkins 2015) with its mesh-less finite mass scheme and utilises the galaxy formation input physics of the state-of-the-art Simba simulation (Davé et al. 2019). The baryon model was re-calibrated because THE THREE HUNDRED initial conditions have a lower resolution than the original SIMBA simulation, and both simulations had different objectives (cosmological run for SIMBA and galaxy cluster for THE THREE HUNDRED). The GRACKLE-3.1 library (Smith et al. 2017) is utilised to implement the processes of radiative cooling, photon heating, and gas ionization. The spatially-uniform ultraviolet background model (Haardt & Madau 2012) and the self-shielding prescription, based on the approach by Rahmati et al. (2013), are employed. Additionally, an H_2 -based star formation model from the MUFASA (Davé et al. 2016) is included. The star formation-driven galactic winds are implemented based on a decoupled two-phase model. This model is also based on MUFASA, but with an additional mass loading factor derived from Anglés-Alcázar et al. (2017b). The chemical enrichment model tracks eleven elements with metals enriched from supernovae Type Ia and Type II and asymptotic giant branch stars. The black hole accretion description is based on two models: torque limited accretion model for cold gas (Anglés-Alcázar et al. 2015, 2017a) and hot gas accretion model based on Bondi (1952). It incorporates three AGN feedback modes: a kinetic subgrid model for both ‘radiative mode’ and ‘jet mode’ with bi-polar ejections, and a kinetic X-ray feedback model following Choi et al. (2012). A more extensive discussion about the baryon model can be found in Cui et al. (2022); Davé et al. (2016, 2019).

Apart from the disparities in their models, it is essential to recognise that the two codes differ in their objectives when comparing simulation outputs to observations. The GADGET-X simulation is tuned to accurately reproduce the gas properties and relations observed in observations, such as the temperature–mass ($T - M$) and integrated Sunyaev-Zeldovich decrement vs. mass ($Y - M$) relations (e.g., Li et al. 2020; Sayers et al. 2023; Li et al. 2023). On the other hand, the GIZMO-SIMBA simulation is calibrated to reproduce galaxy stellar properties, including the total stellar fraction, satellite stellar mass function, and Brightest Cluster Group (BCG) halo mass functions (see Zhang et al. 2022; Cui 2022; Ferragamo et al. 2023, for comparisons between the two simulations). Since the introduction of THE THREE HUNDRED project in Cui et al. (2018), several studies have used this data on many different projects, such as, Haggard et al. (2020a); Ansarifard et al. (2020); de Andres et al. (2022). We refer the readers to these papers for more details about the project.

2.1 The Halo and Sub-halo Catalogues

The simulation data is analyzed using the AHF (Amiga Halo Finder) open-source software (Knollmann & Knebe 2009) to generate halo/sub-halo catalogues. AHF identifies structures hierarchically within cosmological simulations. It detects and locates spherical over-density peaks in the density field of the simulation, consis-

tently considering dark matter, stars, and gas particles. The physical properties of all identified halos are determined based on the gravitationally bound particles. Halo positions are determined based on the over-density peak and the radius R_{200c} . Additionally, sub-structures, referred to as sub-halos, are identified using the same process. Sub-halos are smaller gravitationally bound entities located within the radius R_{200c} of a larger central structure termed the host halo.

AHF searches for connected overdensity regions within the radius R_{200c} of the main halo. These regions are considered potential sub-halos. For each potential sub-halo, AHF determines whether the particles within the overdensity region are gravitationally bound to the main halo. This involves analyzing and comparing the particles' velocities with the local escape velocity obtained using the spherical potential approximation. If the overdensity region is found to be gravitationally bound to the main halo, it is confirmed as a sub-halo. In the following subsection, we will describe the selection procedure of our host halos and their associated sub-halos used in our study.

2.2 Host-halo and Sub-halo Sample Selection

We selected the sample from each simulated cluster region (for both GADGET-X and GIZMO-SIMBA in THE THREE HUNDRED dataset) focusing on three particular redshifts: $z = 0.394$, $z = 0.194$, and $z = 0$. The redshift $z = 0.394$ is primarily selected to enable a close comparison to observed galaxy clusters in M20, which have redshifts in the range $0.2 < z < 0.6$ with the median $z = 0.39$. The two additional redshifts are for the purpose of evolution studies. Host halos with $M_{200c} > 6.5 \times 10^{14} h^{-1} M_{\odot}$ are selected in each simulation region, ensuring that the uncontaminated mass fraction of the high-resolution particles is greater than 0.98⁴. This mass cut is to cover the observed cluster mass range, note that the three cluster masses in M20 are: 1.59 ± 0.36 (MACS J1206.2–0847), 1.04 ± 0.22 (MACS J0416.1–0403) and 2.03 ± 0.67 (Abell S1063) $\times 10^{15} M_{\odot}$ (see Table 1 in Bergamini et al. 2019).

For each host halo identified at three different redshifts in THE THREE HUNDRED project's simulation runs, we further made selections of sub-halos with two scenarios given below:

2D Sub-halos that have $M_{\text{sub}} > 1 \times 10^{10} h^{-1} M_{\odot}$ and are located within a projected distance of less than $0.15R_{200c}$ (where R_{200c} represents the radius of the host halo) from the host-halo centre in the simulation's XY plane, i.e., $R_{2D} < 0.15R_{200c}$.

3D Sub-halos that have $M_{\text{sub}} > 1 \times 10^{10} h^{-1} M_{\odot}$ and are physically located at a distance less than $0.15R_{200c}$ from their host-halo centre, i.e., $R_{3D} < 0.15R_{200c}$.

For the investigation of the cumulative sub-halo mass function and the $M_{\text{sub}} - V_{\text{circ}}$ relation, we considered the sub-halo mass cut mentioned above. However, it's important to note that, in the correlation studies, we applied a significantly higher sub-halo mass cut of $M_{\text{sub}} > 1.27 \times 10^{11} h^{-1} M_{\odot}$ to the dataset. This was done to mitigate potential resolution-related issues that could affect the sub-halos properties. Similarly, we also eliminated any contaminated sub-halos with a low-resolution particle mass fraction greater than 2 per cent. sub-halos without any stars are also excluded from our analysis. Moreover, in GADGET-X, we found some sub-halos with unusually high stellar mass fraction (f_* , is approximately above

0.8) but very low dark matter content close to the host halo's centre ($\approx R_{3D} < 0.05R_{200c}$), and subsequently excluded them from our analysis. However, this issue was not observed in the sub-halos sampled from the GIZMO-SIMBA runs.

The general information regarding our chosen sample is presented in Tables 1 for GADGET-X and 2 for GIZMO-SIMBA. Table 1 presents information on the selected host halos with the higher mass cut, including the number (N_{host} , column 2), the median mass M_{200c} (column 3) of host halos, the median number of sub-halos within $R_{2D} < 0.15R_{200c}$ of each host halo (column 4) and $R_{3D} < 0.15R_{200c}$ (column 6) with their median masses in column 5 and 6 respectively. Additionally, the table also provides the total number of selected sub-halos for $R_{2D} < 0.15R_{200c}$ (column 7) and $R_{3D} < 0.15R_{200c}$ (column 8) for GADGET-X simulated clusters. The different rows show these quantities at the three different redshifts. Similarly, Table 2 reports information for the selected host-halos and sub-halos for simulated clusters at three different redshifts for the GIZMO-SIMBA run.

Based on this dataset of simulated clusters' host-halos and sub-halos from THE THREE HUNDRED dataset, we will commence our investigation to examine whether significant offsets exist between the observations of M20 and the simulations in the context of strong gravitational lensing.

3 SUB-HALO MASS FUNCTION

We begin our analysis by comparing the cumulative sub-halo mass functions predicted by THE THREE HUNDRED clusters to the ones derived from the lens model of the three reference clusters, MACSJ0416, MACSJ1206, and AS1063, in M20. We calculate the sub-halo mass function for each cluster to determine the median cumulative sub-halo mass function at the specified redshifts for the GADGET-X and GIZMO-SIMBA simulations. This is accomplished by utilising the available sub-halo information associated with each cluster. Next, we bin the sub-halos based on their mass, M_{sub} , into logarithmic mass bins and calculate the median value of $N(> M_{\text{sub}})$ for each bin. This process yields the median cumulative sub-halo mass function for the simulated clusters at the respective redshifts. Additionally, we calculate the lower and upper 34% percentiles for $N(> M_{\text{sub}})$ in each logarithmic mass bin as their associated certainty.

Fig. 1 depicts the median cumulative sub-halos mass function $R_{2D} < 0.15R_{200c}$ (left) and $R_{3D} < 0.15R_{200c}$ (right) for both GADGET-X and GIZMO-SIMBA, at three redshifts, $z = 0.394$, $z = 0.194$, and $z = 0$. The grey shaded region in Fig. 1 (left and right) represents the upper and lower 34% quantiles for the cluster at redshift $z = 0.394$ for GADGET-X and GIZMO-SIMBA. Despite employing different approaches, such as using projected 2D distance or considering the actual physical 3D distance between sub-halos and the host-halo centre, the cumulative sub-halo mass function follows a power-law trend when fitted analytically with a power law function, as previously demonstrated in Giocoli et al. (2008). The cumulative sub-halo mass function observed in the GIZMO-SIMBA simulation displays a clearly evident straight power law trend, with a power index almost equal to 1 when compared to the GADGET-X simulation. Upon comparing the results with the observed sub-halo mass functions from M20 obtained through a strong lensing model (represented by black curves with different line styles in Figure 1), we observe consistency between the observations of MACSJ0416 and MACSJ1206 and the results from GIZMO-SIMBA simulated clusters within $R_{2D} < R_{200c}$. For GADGET-X simulated clusters, we find that the sub-halo mass function ($R_{2D} < 0.15R_{200c}$) have a better agreement with obser-

⁴ The fraction is not 100 per cent, for AHF takes BH particles as low-resolution particles. However, changing this fraction does not affect our results.

Table 1. Host halos and sub-halos samples obtained from the GADGET-X simulated clusters dataset. The meaning of each column is indicated in the header (See Section 2.2 for further details). The information presented in the table pertains to sub-halos that are located at distances less than $0.15R_{200c}$. Sub-halo mass threshold of $M_{\text{sub}} > 1.27 \times 10^{11} h^{-1} M_{\odot}$ is used in the table to calculate the statistics.

z	N_{host}	Median M_{200c} [$h^{-1} M_{\odot}$]	Median N_{2D}^{sub}	Median M_{sub}^{2D} [$h^{-1} M_{\odot}$]	Median N_{3D}^{sub}	Median M_{sub}^{3D} [$h^{-1} M_{\odot}$]	Total N_{2D}^{sub}	Total N_{3D}^{sub}
0.394	90	7.97×10^{14}	10	2.62×10^{11}	3	2.78×10^{11}	895	310
0.194	180	8.17×10^{14}	9	2.70×10^{11}	3	2.84×10^{11}	1719	576
0	321	8.46×10^{14}	7	2.57×10^{11}	2	2.49×10^{11}	2631	875

Table 2. Similar to Table 1, but for GIZMO-SIMBA.

z	N_{host}	Median M_{200c} [$h^{-1} M_{\odot}$]	Median N_{2D}^{sub}	Median M_{sub}^{2D} [$h^{-1} M_{\odot}$]	Median N_{3D}^{sub}	Median M_{sub}^{3D} [$h^{-1} M_{\odot}$]	Total N_{2D}^{sub}	Total N_{3D}^{sub}
0.394	82	8.04×10^{14}	15	2.42×10^{11}	6	2.46×10^{11}	1264	488
0.194	169	8.14×10^{14}	14	2.35×10^{11}	5	2.33×10^{11}	2373	966
0	302	8.32×10^{14}	12	2.30×10^{11}	5	2.21×10^{11}	3922	1578

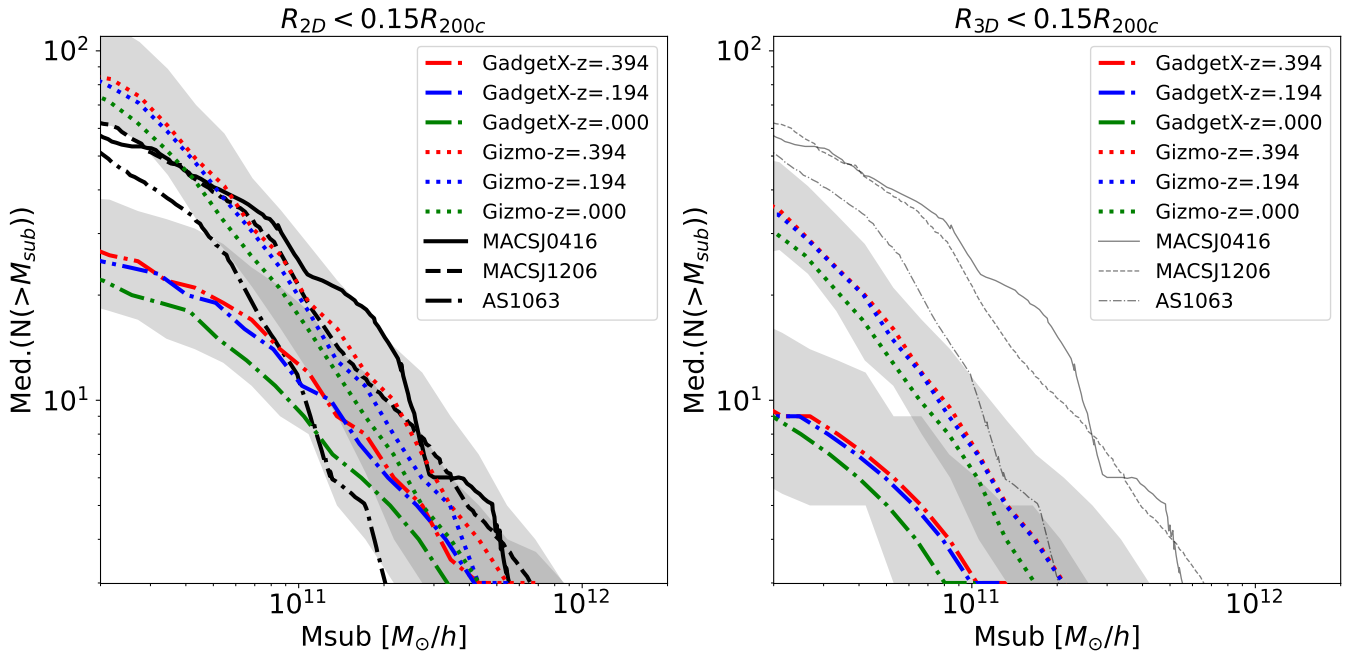


Figure 1. 2D colored (left panel) and 3D (right panel) cumulative sub-halo mass functions. The dotted line style represents the GIZMO-SIMBA simulation results, while dash-dot lines show median cumulative sub-halo mass functions from GADGET-X. The shaded areas show the 16th – 84th percentiles from all clusters at $z = 0.394$. The mass functions of sub-halos in GADGET-X and GIZMO-SIMBA simulations are displayed for three redshifts: $z = 0.394$ (red), $z = 0.194$ (blue), and $z = 0$ (green). The projected results in the left panel used all sub-halos located within a projected 2D distance of $0.15R_{200c}$, i.e., $R_{2D} < 0.15R_{200c}$. On the other hand, the right panel illustrates the results using only sub-halos situated within a physical 3D distance of R_{200c} , i.e., $R_{3D} < 0.15R_{200c}$. In both panels, the same observed sub-halo mass functions from three reference clusters in M20 are presented with black curves with different line styles; see the legend for details.

vation results for sub-halo masses greater than $\sim 8 \times 10^{10} h^{-1} M_{\odot}$. Regarding the low sub-halo mass function at the low-mass end, its baryon model has a stronger resolution dependence⁵ because its sub-halo mass function is closer to the power-law if we don't apply the stellar mass constraint $M_* > 0$ (see also Contreras-Santos et al. 2023, which found many dark sub-halos in GADGET-X.). In the scenario where sub-halos are situated within a radial distance of $R_{3D} < 0.15R_{200c}$, both the GADGET-X and GIZMO-SIMBA simulations exhibit a lower median cumulative sub-halo mass function

compared to the observed results. This discrepancy arises because the observational data inherently captures a 2D projection of the sub-halo distribution, while the condition $R_{3D} < 0.15R_{200c}$ in the simulations takes into account the complete 3D spatial distribution of sub-halos. The projection effect increases the sub-halo numbers by a factor of ~ 2.5 , regardless of the sub-halo masses. Note that we only considered sub-halos within R_{200c} of the host halo for projection. We verified that by applying this constraint (i.e., $R_{3D} < R_{200c}$), we only underestimate the sub-halo mass function for the case of $R_{2D} < 0.15R_{\text{vir}}$ by approximately 2.21% compared to the much larger radial constraint of $R_{3D} < 2.5R_{200c}$. Although the whole volume for the projection case is about five times larger than the 3D

⁵ Though we show the sub-halo mass function down to $\sim 10^{10} h^{-1} M_{\odot}$, it is worth noting that these sub-halos only have around 10 dark matter particles.

case, there are much fewer galaxies/sub-halos at large radius (see [Li et al. 2020, 2023](#), for example). Therefore, using a slightly larger projection distance will not affect this result much. To perform this volume comparison, we directly compared the volume of a sphere having a radius of $0.15 R_{200c}$ with the volume of a cylinder characterized by a radius of $0.15 R_{200c}$ and a height of R_{200c} . Lastly, there is a weak redshift evolution of the sub-halo mass functions in all the simulation samples (see also [Giocoli et al. 2008, 2010](#)), which we will detail in the following subsection.

3.1 The redshift evolution of the sub-halo mass function

It is expected that massive clusters have more sub-halos. As shown in [Table 1](#) and [Table 2](#), the median halo mass slightly increases as redshift drops for both GADGET-X and GIZMO-SIMBA. One should expect a higher sub-halo mass function at $z = 0$ than $z = 0.394$. However, the results in [Figure 1](#) for both GADGET-X and GIZMO-SIMBA and within both R_{2D} and R_{3D} show an opposite evolution, i.e., a lower (fewer sub-halos) sub-halo mass function at $z = 0$ compared to $z = 0.394$. We suspect this could be due to the different halo mass distributions between these redshifts. Therefore, we investigate more on this in this subsection.

To examine the redshift evolution of the sub-halos mass function, we only present the projected results in the 2D case, which include more sub-halos. However, we note here that the R_{3D} results are similar to the R_{2D} ones. The sub-halos mass distribution for all GADGET-X and GIZMO-SIMBA simulated clusters at $z = 0.349$ is shown in the left panels (both a and b) of [Fig. 2](#) with the line colour coding to the cluster mass, as indicated by the colour bar to its right. To show the residual redshift evolution of the sub-halo mass function, we first performed a normalisation step by dividing each host halo's cumulative sub-halo mass function by its own halo mass. This normalisation step eliminates any host halo mass dependence from the cumulative sub-halo mass distribution. We then proceed with the calculation of the median sub-halos mass function by grouping the normalised sub-halos mass in logarithmic mass bins and then calculating median $N(> M_{sub})/M_H$ in each bin. The right panel of [Fig. 2](#) shows the redshift evolution of the normalised sub-halo mass distribution predicted by the simulations for both GADGET-X and GIZMO-SIMBA. The plot clearly illustrates the evolution of the sub-halo mass function as the redshift decreases from $z = 0.349$ to $z = 0$. The figure shows that, within a given parent halo, a greater number of sub-halos are expected to be observed at earlier times when they are dynamically young and less concentrated. This similar inference about the redshift evolution of the sub-halos mass aligns with the findings presented in [Gao et al. \(2004\)](#) and [Gao et al. \(2011\)](#). However, here we notice that the evolution we observed in our hydro-dynamical simulations is milder compared to the earlier studies of dark matter-only simulations. Interestingly, the same evolution trend for hydro-dynamical simulations was also reported in works such as [Ragagnin et al. \(2019\)](#), [Ragagnin et al. \(2022\)](#), and [Despali & Vegetti \(2017\)](#). This observation is further supported by the Median N_{2D}^{sub} and Median N_{3D}^{sub} columns in [Tables 1](#) and [2](#) respectively. Moreover, upon examining [Table 2](#) for GIZMO-SIMBA, we observe a general decreasing trend in the sub-halo mass (check M_{sub}^{2D} and M_{sub}^{3D} from redshift $z = 0.394$ to $z = 0$). We have also verified that the same evolutionary trend for the sub-halo mass function is observed when considering a higher redshift snapshot with a value greater than $z = 0.394$. Moreover, the evolution of R_{200c} for a fixed halo mass between $z = 0$ and an arbitrary redshift z is governed by the equation, $\frac{R_{200c}(z=0)}{R_{200c}(z)} = (H(z)/H_0)^{2/3}$. This ratio indicates how the volume slightly increases at low redshift as a result

of variations in the critical over-density, which can be expressed as $\Omega_m(1+z)^{1/3} + \Omega_\Lambda$. This, the pseudo-halo mass evolution, partly leads to the decrease of the satellite number with the R_{200c} at $z = 0$. This is because the redshift evolution in [Figure 2](#) is much larger than this density change.

4 CUMULATIVE SUB-HALO V_{CIRC} FUNCTION

In this section, we will calculate and compare the cumulative sub-halo V_{circ} function for both the GADGET-X and GIZMO-SIMBA simulations at three different redshifts: $z = 0.394$, $z = 0.194$, and $z = 0$. To estimate each sub-halo V_{circ} in both GADGET-X and GIZMO-SIMBA simulations, we used the output profiles generated by AHF ([Knollmann & Knebe 2009](#)). The output files from the AHF contain radial profiles for halo/sub-halo various properties such as mass, density, rotation curve, escape velocity, etc. Here, we only used the rotation curve of each sub-halo to estimate V_{circ} in both GADGET-X and GIZMO-SIMBA at the three redshifts. The circular velocity, denoted as V_{circ} for a sub-halo is determined by identifying the maximum circular velocity at radii greater than zero, ensuring convergence and which is dominated by two-body collisions according to the criterion of [Power et al. \(2003\)](#). The rotation curve for halo/sub-halos is calculated inclusively considering both baryons and dark matter particles in the AHF profile file. We have verified that this value is compatible with the one in the AHF halo properties.

We calculate the sub-halo V_{circ} function for each host cluster to determine the median cumulative sub-halo V_{circ} function at the specified redshifts for both GADGET-X and GIZMO-SIMBA simulations. To calculate the median sub-halo V_{circ} function, we interpolated the individual sub-halo V_{circ} functions for each host halo at given V_{circ} values, and then calculated the median value of $N(> V_{circ})$ using all the interpolated profiles. This process yields the median cumulative sub-halo V_{circ} function for the simulated clusters at the respective redshifts.

[Figure 3](#) illustrates the median cumulative sub-halo V_{circ} function for both GADGET-X and GIZMO-SIMBA simulations at three different redshifts: $z = 0.394$, $z = 0.194$, and $z = 0$. The left panel shows the function for $R_{2D} < 0.15R_{200c}$, while the right panel shows it for $R_{3D} < 0.15R_{200c}$. In [Figure 3](#), the shaded grey region represents the upper and lower 34% percentiles for clusters at redshift $z = 0.394$ in both GADGET-X and GIZMO-SIMBA simulations. The V_{circ} functions for GIZMO-SIMBA are higher compared to GADGET-X for both $R_{2D} < 0.15R_{200c}$ and $R_{3D} < 0.15R_{200c}$. Once more, we notice that the projection effect leads to an approximately twofold increase in the sub-halo count in both the GADGET-X and GIZMO-SIMBA simulations. Additionally, we noticed a subtle redshift evolution in the cumulative sub-halo V_{circ} function for both GADGET-X and GIZMO-SIMBA, which agrees with the result of the sub-halo mass function considering the positive correlation between V_{circ} and M_{sub} , further discussed below.

5 $M_{SUB} - V_{CIRC}$ RELATION

In this section, we investigate the discrepancy between the concentration of sub-halos in THE THREE HUNDRED simulations and the lensing results of M20. Following [M20](#), [Ragagnin et al. \(2022\)](#); [Bahé \(2021\)](#), we employed the $M_{sub}-V_{circ}$ relationship as a metric to infer the concentration of sub-halos within the clusters. The sample of selected sub-halos for both GADGET-X and GIZMO-SIMBA remains unchanged. To derive the $M_{sub}-V_{circ}$ relationship, we initially divide the sub-halo masses into logarithmic mass bins and subsequently calculate the

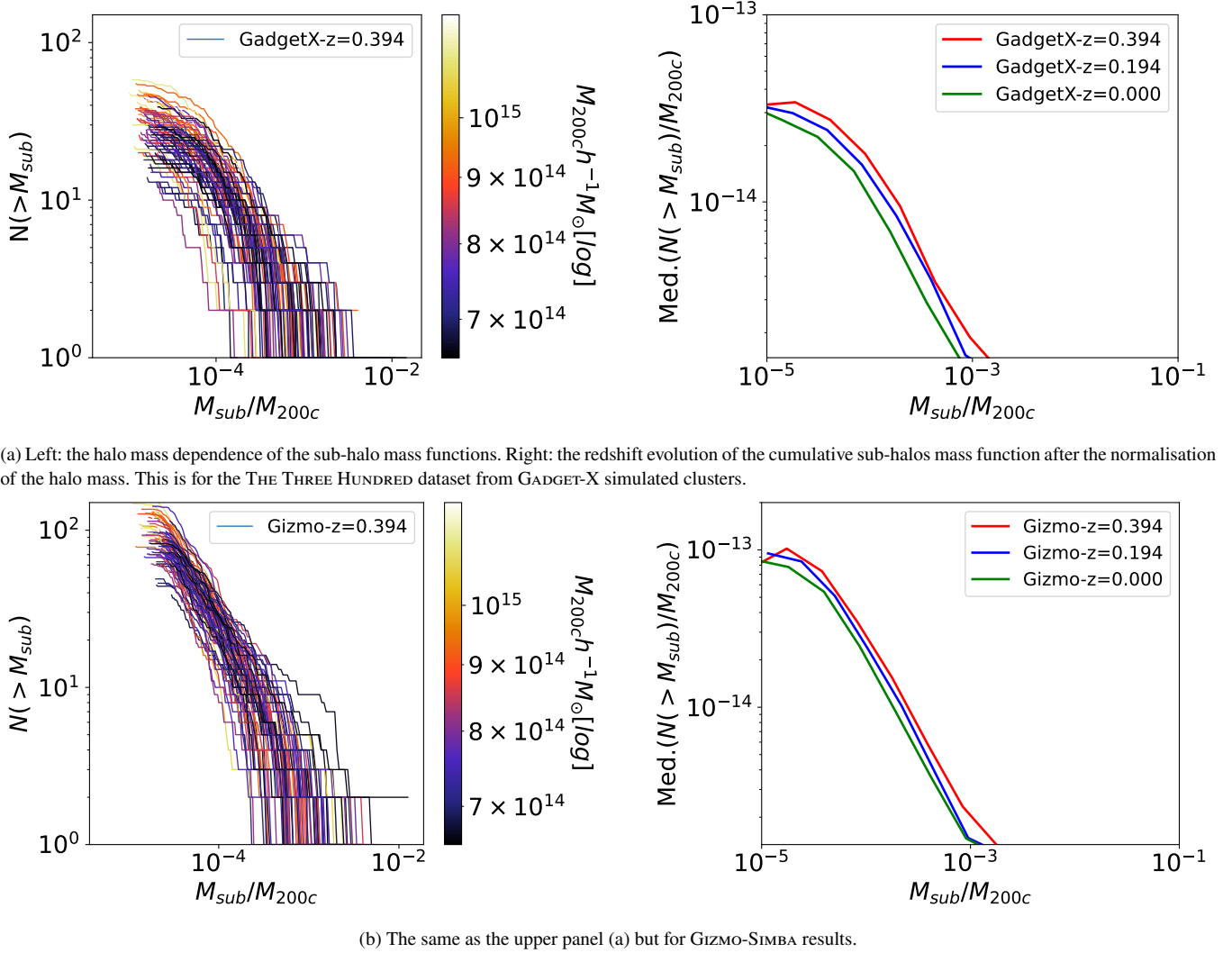


Figure 2. In panels (a and b, left), we illustrate the unnormalized sub-halo mass functions at $z = 0.394$, demonstrating their dependence on halo mass. The right panels (a and b) display the corresponding cumulative sub-halo mass functions for the normalized sub-halo mass function at redshift $z = 0.394$, along with the normalized sub-halo mass functions at $z = 0.194$ and $z = 0$. Further details regarding these plots are provided in sub-captions (a) and (b).

median V_{circ} for each respective bin. $M_{\text{sub}}-V_{\text{circ}}$ relation is then obtained by plotting the middle values M_{sub} in each bin with respect to the corresponding median values of V_{circ} for each bin. This procedure was repeated for both GADGET-X and GIZMO-SIMBA simulations at the three redshifts considered in our study.

In Figure 4, we present the $M_{\text{sub}}-V_{\text{circ}}$ relationship for the sub-halos from GADGET-X and GIZMO-SIMBA simulated clusters and compare it with the relation of the observed clusters derived by M20. The left panel of Figure 4 presents the projected results while the right panel shows the 3D case. We use different colors to show the $M_{\text{sub}}-V_{\text{circ}}$ relations (for both GADGET-X and GIZMO-SIMBA) at three different redshifts, namely $z = 0.394$, $z = 0.194$ and $z = 0$. When sub-halos follow the distance constraint $R_{2D} < 0.15R_{200c}$, both GADGET-X and GIZMO-SIMBA simulated clusters exhibit consistently lower V_{circ} values compared to the fitting line from observation. Sub-halos located at the periphery (i.e. $R_{3D} \approx R_{200c}$) for the 2D case $R_{2D} < R_{200c}$, cause the simulation's $M_{\text{sub}}-V_{\text{circ}}$ relation to shift downward compared to the observed relation. GIZMO-SIMBA, though, shows slightly higher V_{circ} than GADGET-X. Furthermore, GIZMO-SIMBA tends to have a weak redshift evolution as a higher V_{circ} at $z = 0.394$ com-

pared to $z = 0$, while no redshift evolution is presented in GADGET-X. Similarly, the same conclusions are reached for the case when $R_{3D} < R_{200c}$, albeit that both seem to become closer to the observation fitting line, which is in agreement with M20 and our later correlation studies. Even after considering the sub-halos of the 10 most massive host halos, the discrepancy between the observed and simulated V_{circ} values persists. We do not see significant differences between different sub-halo masses regarding the distances to the fitting line, although the shaded regions seem larger, thus closer to the fitting line, at higher sub-halo masses. We also emphasize that the disparity between the $M_{\text{sub}}-V_{\text{circ}}$ relations of GADGET-X and GIZMO-SIMBA is primarily limited to the lower sub-halo mass range. For sub-halos with $M_{\text{sub}} > \approx 10^{12}h^{-1}M_{\odot}$, they exhibit a notable degree of agreement. As we have noticed, the sub-halos at the lower halo mass range can be unresolved. Based on our analysis of the sampled data, we have not identified any significant deviations or trends in the $M_{\text{sub}}-V_{\text{circ}}$ relation that can be directly attributed to unresolved sub-halos in the lower sub-halo mass range. Nevertheless, we acknowledge that further investigations with higher-resolution simulations is necessary to gain a more complete insight into how

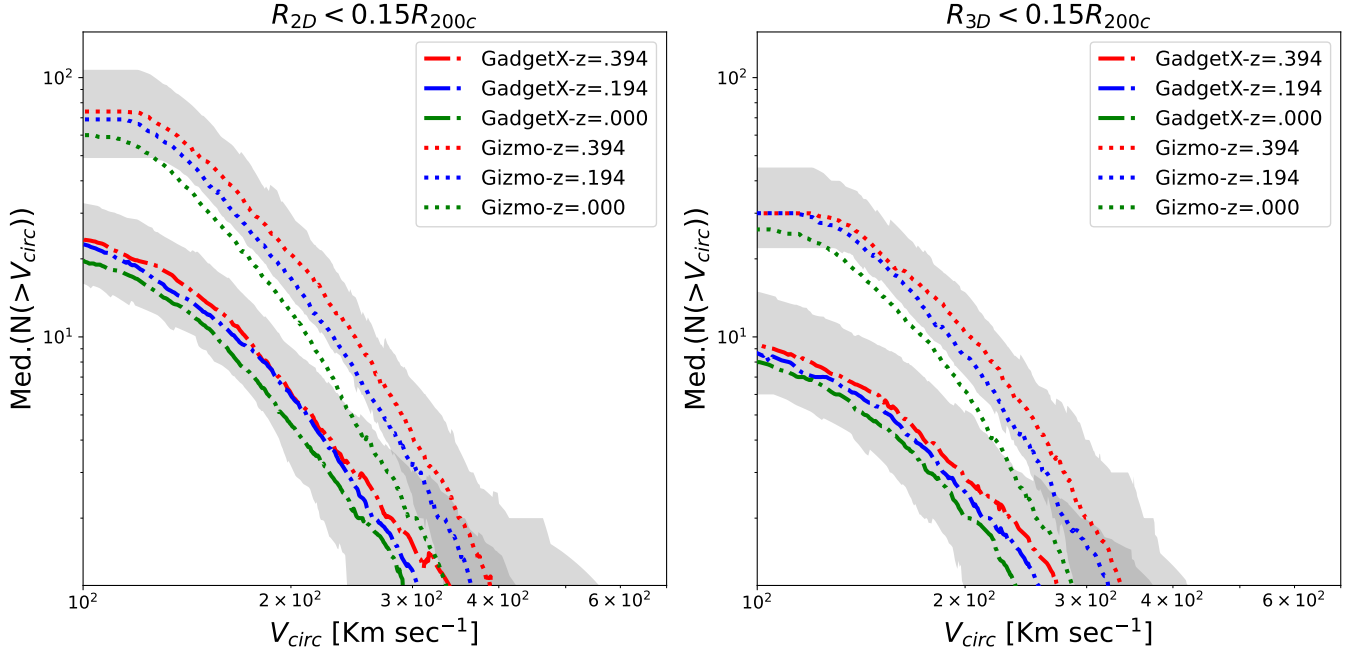


Figure 3. 2D (left panel) and 3D (right panel) cumulative sub-halo V_{circ} functions. The dotted line style represents the GIZMO-SIMBA simulation results, while dash-dot lines show median cumulative sub-halo V_{circ} functions from GADGET-X. The shaded areas show the 16th – 84th percentiles from all clusters at $z = 0.394$. The V_{circ} functions of sub-halos in GADGET-X and GIZMO-SIMBA simulations are displayed for three redshifts: $z = 0.394$ (red), $z = 0.194$ (blue), and $z = 0$ (green). The projected results in the left panel used all sub-halos located within a projected 2D distance of $0.15R_{200c}$, i.e., $R_{2D} < 0.15R_{200c}$. On the other hand, the right panel illustrates the results using only sub-halos situated within a physical 3D distance of R_{200c} , i.e., $R_{3D} < 0.15R_{200c}$. We also mention that we employed sub-halos with masses greater than $10^{10}h^{-1}M_{\odot}$ when computing the V_{circ} functions for both GADGET-X and GIZMO-SIMBA.

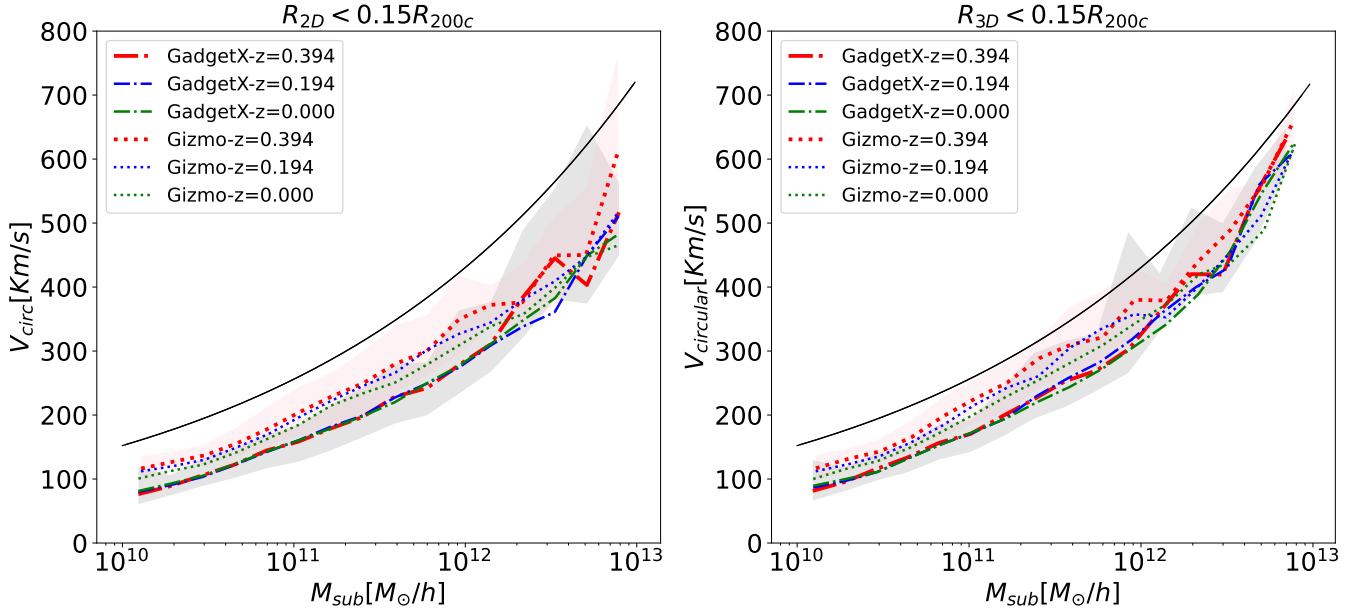


Figure 4. The relationship between sub-halo mass (M_{sub}) and maximum circular velocity (V_{circ}) for the 2D projected sub-halos on left panel and for the 3D one on the right panel. The black solid line is observed fitting relation from M20 in both panels for reference. The $M_{\text{sub}}-V_{\text{circ}}$ relation for the two simulations is distinguished by distinct line styles, with dashed-dot representing GADGET-X and dotted representing GIZMO-SIMBA. The $M_{\text{sub}}-V_{\text{circ}}$ relation in GADGET-X and GIZMO-SIMBA simulations are displayed for three redshifts: $z = 0.394$ (red), $z = 0.194$ (blue), and $z = 0$ (green). The light grey and red shaded regions depict the upper and lower 34% quantile regions computed in each logarithmic mass bin at redshift $z = 0.394$ for GADGET-X and GIZMO-SIMBA, respectively.

unresolved sub-halos in this mass range might affect the relation. We also observed that the simulated $M_{\text{sub}} - V_{\text{circ}}$ relationship for sub-halos with masses $M_{\text{sub}} \lesssim 10^{11} h^{-1} M_{\odot}$, which is the most crucial mass range for GGSF events (Ragagnin et al. 2022), differs constantly from observations. Conversely, the $M_{\text{sub}} - V_{\text{circ}}$ relation in simulations for the massive sub-halos, $M_{\text{sub}} > 4 \times 10^{11} h^{-1} M_{\odot}$, becomes closer to observed relation by varying the baryon parameters, as noted also in Bahé (2021). However, it's worth noting that this specific range of sub-halo masses is notably higher than what is observed, as highlighted in Ragagnin et al. (2022). Though we have a much larger sample and observe that the lines are closer to the observation line at the most massive sub-halo mass range, the discrepancy at the low sub-halo mass end remains unsolved. Note that the resolution, which could affect this statement for our simulations, given by the checks from Ragagnin et al. (2022), Bahé (2021) and our examinations of the high-resolution the300 clusters, does not significantly impact the $M_{\text{sub}} - V_{\text{circ}}$ relation. Therefore, it is still unclear whether this can be solved by varying baryon models or not. The difference between GIZMO-SIMBA and GADGET-X suggests that this may be the case. In the following section, we aim to investigate the influence of sub-halo properties on the $M_{\text{sub}} - V_{\text{circ}}$ relation, where we examine how these properties relate to the difference between the V_{circ} obtained from the simulation and the one derived from observed fitting relations. This difference serves as a measure of the goodness of fit to the $M_{\text{sub}} - V_{\text{circ}}$ relation.

5.1 The effects of the sub-halo properties on $M_{\text{sub}} - V_{\text{circ}}$ relation

While GIZMO-SIMBA appears to be somewhat closer to the observed fitting line than GADGET-X, the deviation from the observational results remains substantial. This is particularly pronounced in the case of the projected data, which holds greater importance in the observational context. It is interesting to see that different baryon models indeed give slightly different results, which means there may be a cure for this discrepancy by better calibrating the baryon models. Therefore, in order to understand the impact of sub-halo properties on the $M_{\text{sub}} - V_{\text{circ}}$ relation, we perform a Spearman correlation analysis between the different physical properties of the sub-halos and the residual for all sub-halos in the $R_{2D} < 0.15 R_{200c}$ case. The Spearman correlation test involves converting the data into ranks and then calculating the correlation between the ranks of the two variables. This Spearman correlation analysis between the different physical properties of the sub-halos and the residual not only provides more statistics, but also presents a consistent comparison to the observation result. The residual ds is calculated for each sub-halo by finding the distance between its V_{circ} value obtained from the fitting line at its sub-halo mass $V_{\text{circ}}^{\text{fit}}$ and the one derived from the simulations $V_{\text{circ}}^{\text{sim}}$, it is further normalised to the fitted line value:

$$ds = \frac{V_{\text{circ}}^{\text{sim}} - V_{\text{circ}}^{\text{fit}}}{V_{\text{circ}}^{\text{fit}}}. \quad (1)$$

Note that, we only use sub-halos with $M_{\text{sub}} > 1.27 \times 10^{11} h^{-1} M_{\odot}$ to calculate these correlation coefficients. This is attributed to the potential influence of simulation resolutions on certain sub-halo properties, as sub-halos below this range roughly consist of fewer than 100 dark matter particles. Apart from identifying halos and their corresponding sub-halos, AHF (Knollmann & Knebe 2009) also provide many physical properties associated with them. Here, we investigate these quantities which should have the most effects on the $M_{\text{sub}} - V_{\text{circ}}$ relation. The sub-halo properties analysed with the Spearman correlation

test include the Bullock Spin parameter, which is a measure of the spin of the sub-halo based on Bullock et al. (2001), and the Peebles Spin parameter, which is another measure of the sub-halo's spin based on a different definition by Peebles (1969). The dimensionless spin parameter in Peebles (1969) is calculated as $\sqrt{E}|J|/GM^{\frac{5}{2}}$, where E represents the total energy, J denotes the angular momentum, and M stands for the mass of the sub-halo or halo. However, estimating this quantity poses challenges as it requires determining the total energy E from simulations and observations. The difficulty arises from the necessity to compute the gravitational potential energy, which, in turn, relies on obtaining accurate information about the mass distribution. To overcome this problem, an alternative dimensionless spin parameter was proposed in Bullock et al. (2001). It is calculated as $|J|/\sqrt{2}MRV$, where $|J|$ denotes the angular momentum, M is the mass of the sub-halo, R is the virial radius, and V is the virial circular velocity given by $V = \sqrt{\frac{GM}{R}}$. The measurements of J , M , and V are all confined to the virial radius R . This makes this spin definition especially attractive since it solely depends on the material within R , enabling its calculation for individual components. Hence, using this definition, the radial distribution of the spin is straightforward.

Furthermore, the analysis takes into account the baryonic mass fraction (f_b), which represents the proportion of baryonic matter (ordinary matter i.e. gas and stellar content) within the sub-halo. The centre of mass offset parameter (COM_offset), the distance between the centre of mass of the sub-halo and its density peak, is also considered. This is normally used as an indicator of the object's dynamical state (see Cui et al. 2017, for example).

In addition to that, we further calculate some galaxy and sub-halo properties that may be directly linked to the ds , but not provided by AHF. These properties included in the analysis are the physical distance between the host-halo and the sub-halos (R_{3D}), the galaxy's half-stellar mass radii, the galaxy's stellar age, which is the mass-weighted mean of all-star particles within the half-stellar mass radius, the sub-halo half-mass radii and the galaxy/sub-halo concentrations. As it is very difficult to decide the density profiles for these sub-halos and therefore to estimate their concentration, it is very common to use the ratio of two radii, R_{80} and R_{20} , as an indicator of the concentration. Here, R_{80} marks the radius where 80 per cent of the total (stellar) mass of the sub-halo (galaxy) is included. With a similar definition for R_{20} , one would expect a more concentrated density profile should have a higher ratio R_{80}/R_{20} .

The correlation between the physical properties of the sub-halos (for both GADGET-X and GIZMO-SIMBA) and the residual ds is depicted in Fig. 5. It is clear that both simulations generally agree on the (anti-)correlation between ds and sub-halo/galaxy properties. Namely, the higher Spin, COM offset, galaxy/sub-halo half mass radius and concentration, further from cluster centre and galaxy concentration, the further distance to the fitted $M_{\text{sub}} - V_{\text{circ}}$ relation. We displayed the Spearman correlation coefficient only for the Bullock spin parameter, which is more robust. The Peebles spin parameter showed a similar trend with a comparable correlation coefficient. At the same time, the older galaxy age (formed earlier) and sub-halos baryonic mass fraction will bring the simulated sub-halo V_{circ} closer to the observed relation. We also examined the correlation trend for the Stellar mass fraction, which exhibited a positive correlation with the residual ds . It displayed a closely similar magnitude to the baryon fraction. This is not surprising given that simulated satellites have virtually no gas; therefore, these two fractions are expected to be nearly identical. It is worth noting that the most significant sub-halo properties are galaxy stellar age, R_{3D} distance, sub-halo half mass radius, and baryon fractions. The Spearman correlation trends between ds

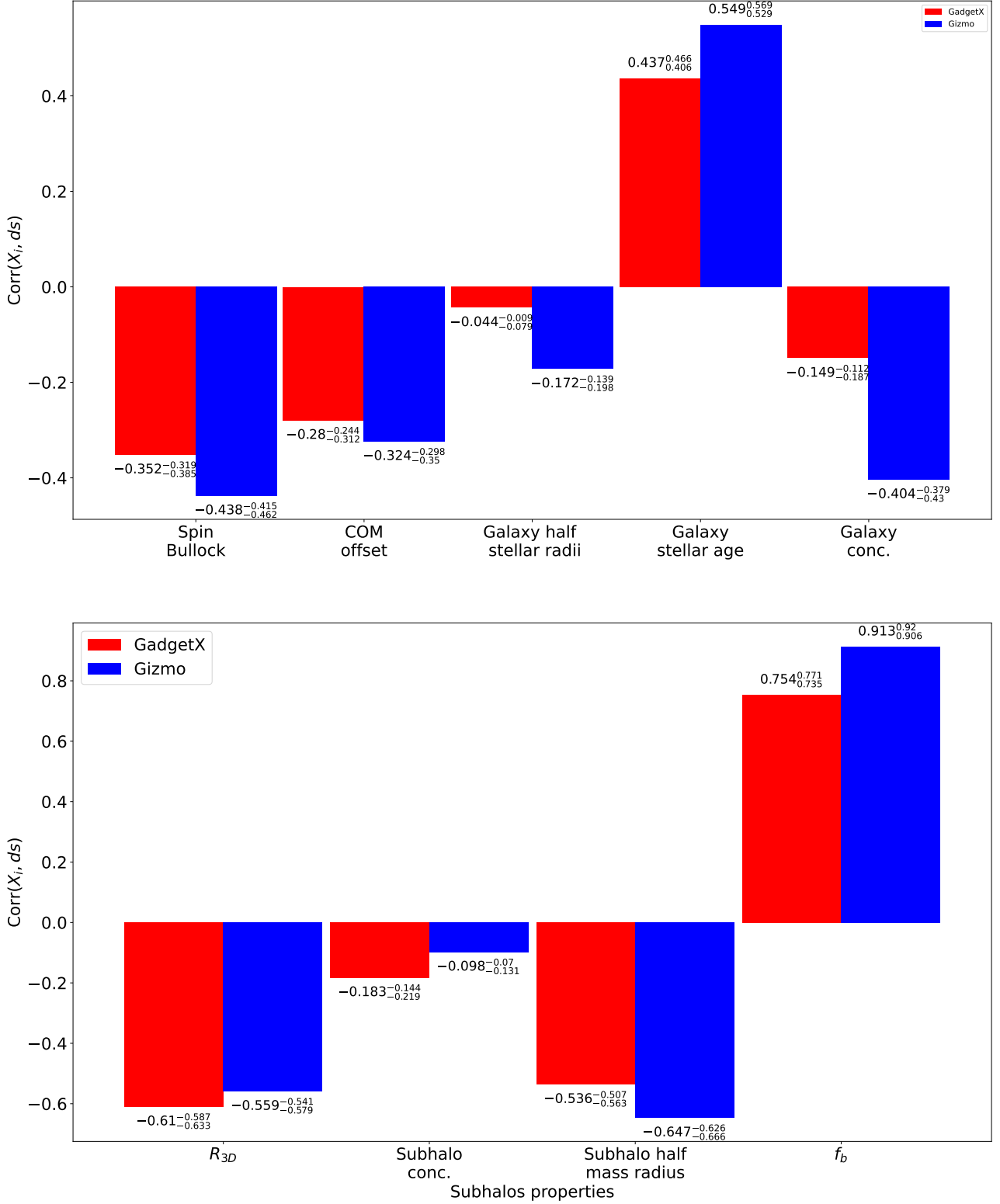


Figure 5. The Spearman correlation coefficient between the physical properties of sub-halos and the residuals ds . The residual ds is computed as the distance from the sub-halo's circular velocity obtained from the simulation to the one predicted by the observed relation. To distinguish between the two simulations, we use the red bar plots for the results of GADGET-X and the blue bar plots for the results of GIZMO-SIMBA, respectively. The values of the bar plot are the Spearman correlation coefficient between the sub-halo residual ds and various sub-halo properties. $\text{Corr}(X, ds)$ defines the Spearman correlation coefficient between the physical property X of sub-halos and the residual ds . This parameter is obtained by rank-ordering the sub-halo property X and the residual ds , and then calculating the Pearson coefficient based on this rank-order list. The value of this parameter falls between -1 and 1. For the Spearman correlation studies, we chose sub-halos that meet the following criteria: their mass $M_{\text{sub}} > 1.27 \times 10^{11} h^{-1} M_{\odot}$, and their 2D projected distance $R_{2D} < 0.15 R_{200c}$. The Spearman correlation coefficients are accompanied by superscripts and subscripts denoting upper 84% and lower 16% uncertainties, respectively.

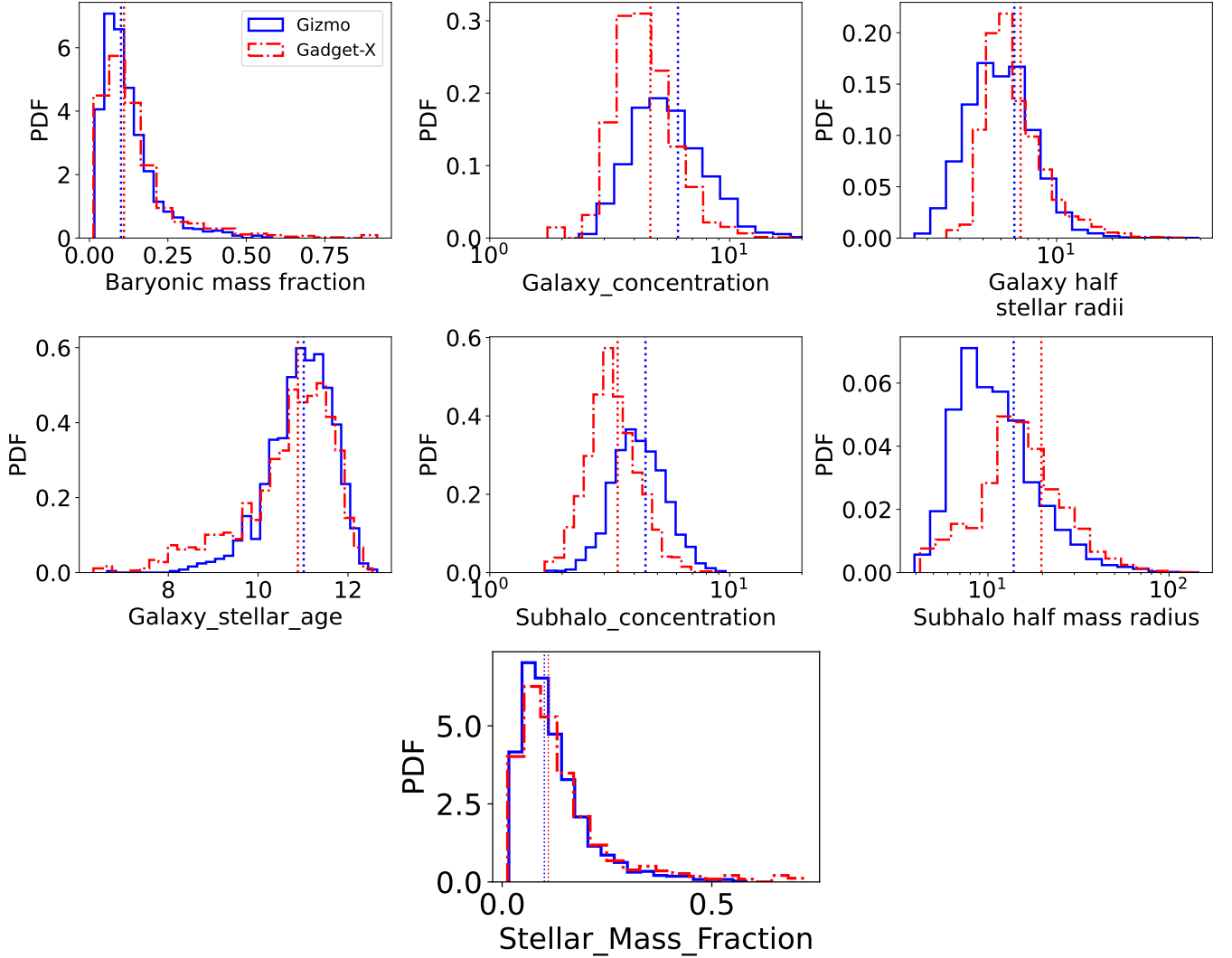


Figure 6. The probability density functions (PDFs) of the baryonic mass fraction, galaxy concentration, galaxy half stellar radii, galaxy stellar age, sub-halo concentration and sub-halo half mass radii from top left to bottom right for both GADGET-X (red dash-dot steps) and GIZMO-SIMBA (blue solid steps). The distributions are presented in either linear or logarithms based on their spread ranges. The dotted vertical lines in each plot correspond to the median values of the distributions. For the comparison of sub-halo properties between the two simulations, we selected sub-halos that meet the following criteria: their mass, $M_{\text{sub}} > 1.27 \times 10^{11} h^{-1} M_{\odot}$, and their 2D projected distance, $R_{2D} < 0.15 R_{200c}$.

and R_{3D} , as well as ds and f_b , obtained from our analysis, have also been reported in M20 and Bahé (2021), respectively. The positive correlation between ds and galaxy age suggests early galaxy formation in simulations will provide a better agreement, which is also consistent with the recent JWST observations on the very high-redshift galaxies (see Naidu et al. 2022; Finkelstein et al. 2022, for example). It is also interesting to note that in the GIZMO-SIMBA simulation, both the gas fraction (f_b) and galaxy age are more strongly positively correlated to ds compared to GADGET-X. For the negative correlation between ds and the sub-halo half mass radius, it is very easy to understand: the larger radius, the puffier the sub-halo is, therefore, the lower V_{circ} . Naively, we also expect that the sub-halo half mass radius will be anti-correlated with the sub-halo concentration. By directly looking at the coefficient between the sub-halo half mass radius and concentration, which is also negatively correlated, we suspect that this is caused by different sub-halo masses for the anti-correlation at a fixed sub-halo will be diluted by plotting all the sub-halos together. Therefore, we state that the mentioned correlation between sub-halo

half mass radius and concentration is not shown 6. Furthermore, this is also applied to the galaxy concentration parameter. This simple definition of concentration may not serve our purpose well here. We also emphasize that this correlation study holds greater relevance in the context of sub-halos with $M_{\text{sub}} > 1.27 \times 10^{11} h^{-1} M_{\odot}$, as we applied this mass threshold to mitigate resolution-related effects that can influence the physical properties of sub-halos. Hence, no definitive conclusions can be drawn regarding the influence of sub-halo properties on the $M_{\text{sub}} - V_{\text{circ}}$ relation for sub-halos falling below the mentioned mass threshold.

In addition to examining the correlations with ds , which highlights the individual sub-halo properties' effect, we also compared the distribution of sub-halo properties between GADGET-X and GIZMO-SIMBA in Figure 6. The distributions of galaxy/sub-halo properties are presented with the 1D probability density functions for both simulations. Through these comparisons, we expected to further understand the model differences between the two simulations and how

they impact the $M_{\text{sub}} - V_{\text{circ}}$ relation. In Figure 6, only 6 interesting and important sub-halo properties are picked to show.

First, the sub-halos in the simulated clusters of GADGET-X contain a marginally higher amount of baryonic content compared to those in GIZMO-SIMBA. Note that the distribution difference is larger when including low-mass sub-halos. The positive correlation illustrated in Figure 5 indicates that as the baryon fraction increases, the simulation's $M_{\text{sub}} - V_{\text{circ}}$ relation aligns more closely with the observed fitting relation. The explanation behind this is: the inclusion of baryons through tidal stripping leads to an observed offset towards higher V_{circ} values in the $M_{\text{sub}} - V_{\text{circ}}$ relation (Bahé 2021), which is also supported by the presence of sub-haloes with increased baryonic content results from the removal of dark matter in galaxies with the stellar mass is largely preserved (Armitage et al. (2019); Bahé et al. (2019); Joshi et al. (2019)). However, this result seems to contradict the conclusion that GIZMO-SIMBA is closer to the fitting line than GADGET-X while their baryon fractions are very similar. We suspect the baryon fraction is only a sufficient condition, not a necessary condition to bring up the V_{circ} . Similar to the baryon fraction, the galaxy age distributions between GADGET-X and GIZMO-SIMBA are also very similar with a slight excess of young galaxies in GADGET-X. Therefore, the similarity of the two sub-halo properties between GADGET-X and GIZMO-SIMBA indicates that other quantity differences are the key to explaining the differences in the $M_{\text{sub}} - V_{\text{circ}}$ relation. They are the sub-halo/galaxy half-mass radii and concentrations: it is clear that GIZMO-SIMBA has smaller half-mass radii, thus a higher concentration of both galaxy and sub-halo compared to GADGET-X. This is in agreement with Meneghetti et al. in prep. which found that the GGLS signal is also higher in GIZMO-SIMBA than GADGET-X, albeit that is still about a few times lower than observation. To boost the V_{circ} , as well as the GGLS signal, we will need even more compact sub-halos/galaxies. To achieve that goal, we suspect an even earlier galaxy formation may bring the simulation closer to observation.

5.2 Global cluster properties impact on $M_{\text{sub}} - V_{\text{circ}}$ relation

The next step in our analysis is to investigate the influence of the global properties of the host halo on the $M_{\text{sub}} - V_{\text{circ}}$ relationship. This investigation is to provide some hints on whether the selected clusters in observation are biased or not. In order to determine any potential impact, we provide a similar study on the Spearman coefficient between the physical properties of the host halos and the global residual \overline{ds} . Here, the global residual \overline{ds} for each host halo is computed by averaging all its sub-halos' ds , which are measured in the previous section.

In Figure 7, we show the coefficient between \overline{ds} and these four selected cluster properties: cNFW, Bullock spin parameter, COM offset and total baryon fractions. Additionally, the analysis considers the Navarro-Frenk-White profile (Navarro 1996) dimensionless concentration parameter (cNFW), which characterises the concentration of the sub-halo's density profile. The concentration parameter, denoted as cNFW, is typically determined by fitting a Navarro-Frenk-White profile to the halo density. It describes how the density of the halo changes with radial distance from its centre. Here, we simply use the concentration parameter in AHF calculated by following the approach of Prada et al. (2012). They utilise the circular velocity (V_{circ}) and the circular velocity at the virial radius, which is defined in terms of the halo's virial mass and radii. All the other halo properties are introduced in the previous section.

Besides the cNFW parameter, the two simulations show similar correlations with the \overline{ds} . GADGET-X suggests that concentrated halos tend to give a lower $M_{\text{sub}} - V_{\text{circ}}$ relation, while GIZMO-SIMBA sug-

gests the opposite. However, neither shows a strong relation with \overline{ds} . Both Bullock and Peebles defined spin parameters negatively correlate with \overline{ds} indicating slow-rotating halos tend to be closer to the observed fitting line. We report the more robust Bullock spin parameter in Figure 7. Again, the correlation is not very strong. The highest coefficient is the COM, which suggests that the relaxed halos tend to agree with observation better. This can be understood as this: the relaxed cluster tends to form earlier (see Mostoghiu et al. 2019, for example, for the relations of cluster dynamical state with halo formation time and concentration), and the sub-halos inside tend to have a longer time for stripping, thus only the core regions are remaining, which will have a shorter half-mass radius with higher V_{circ} . However, it is worth note that one cluster, MACSJ0416, in M20, seems to be unrelaxed. This seems contract to our previous prediction. However, we argue that the majority of the sample in M20 (see also Meneghetti et al. (2022)) also are more relaxed. While the simulation sample is more balanced, see De Luca et al. (2021); Zhang et al. (2022).

The positive correlation between \overline{ds} and the halo baryon fraction is in agreement with the correlation result for sub-halos. It is expected that the higher halo baryon fraction connects with a higher sub-halo baryon fraction. However, it is unclear which is the determined reason: the baryon-rich halo merged into the host halo to bring more baryons or the host halo is baryon rich with the sub-halos can retain their baryon longer. It is naturally to think that a higher halo baryon fraction would induce stronger ram pressure with potentially stronger tidal forces, thus leads to a lower baryon fraction in the sub-haloes. It is known recently that the gas in the infalling halos is easily stripped out (Haggar et al. 2020b), even before reaching the virial radius of the cluster, this can also happen to the infalling groups as well (Haggar et al. 2023). There the baryon fraction for the satellite galaxies are dominated by stars. On the other hand, the galaxy is more concentrated compared to dark matter, thus less easy get stripped (see Contreras-Santos 2023 in prep.). Therefore, the two high baryon fractions are actually consistent, because the stronger stripping will only remove more dark matter particles and result in a higher subhalo baryon fraction.

6 CONCLUSIONS

The study by M20 examined the gravitational lensing properties of galaxy clusters and their sub-halos, revealing a significant discrepancy between observed clusters and hydrodynamic simulations within the Λ CDM cosmology. Notably, observed clusters exhibited a much higher probability of Galaxy-Galaxy Strong Lensing (GGLS) than simulated clusters. Moreover, they utilized maximum circular velocities (V_{circ}) of sub-halos as a metric to assess compactness, finding that sub-halos in observed clusters had higher V_{circ} values compared to those in mass-matched clusters from simulations. This suggests that galaxies in observed clusters are more efficient at lensing background sources and are more compact than those in the simulations. In this study, we thoroughly investigated the discrepancy between the simulations and observations discussed in M20.

In our study, we used simulated clusters from the THE THREE HUNDRED project Cui et al. (2018, 2022) with masses $M_{200} > 6.5 \times 10^{14} h^{-1} M_{\odot}$. We aimed to compare these simulated clusters with the observations of three primary reference clusters of M20 that have a median redshift of $z = 0.39$. We selected a sample of 90 host clusters from the GADGET-X simulation and 82 host clusters from the GIZMO-SIMBA simulation at a redshift of $z = 0.394$ to compare it fairly with observations of M20. We then expanded our analysis by including host clusters at two additional redshifts:

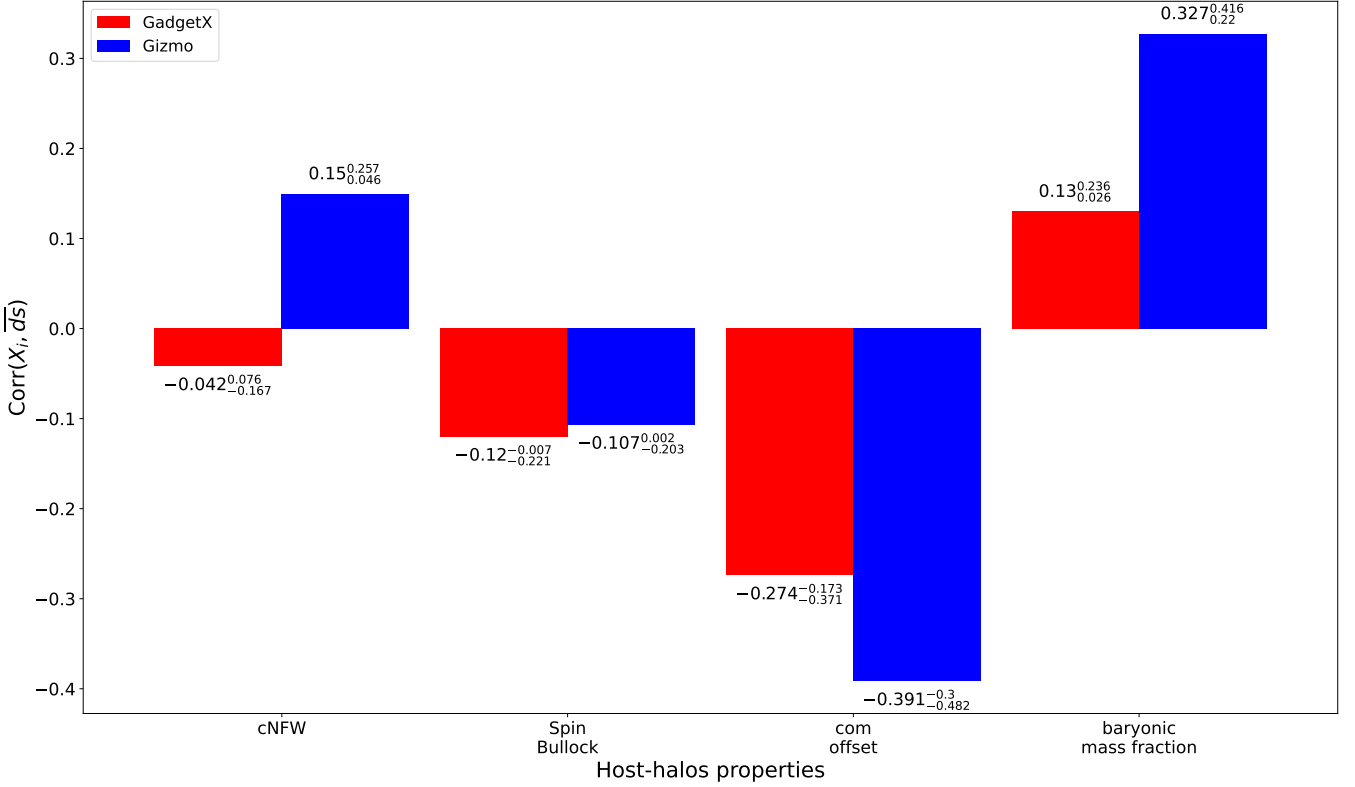


Figure 7. Similar to Figure 5, but for the correlation between the cluster properties and global residuals (\overline{ds}). This correlation can be used to infer the impact of cluster/host-halo physical properties on the $M_{\text{sub}} - V_{\text{circ}}$ relationship. Once again, we selected sub-halos from the host clusters that met the following criteria: their mass, $M_{\text{sub}} > 1.27 \times 10^{11} h^{-1} M_{\odot}$, and their 2D projected distance, $R_{2D} < 0.15 R_{200c}$.

$z = 0.194$ and $z = 0$ for evolutionary studies. The selected clusters at $z = 0.194$ for GADGET-X and GIZMO-SIMBA are 180 and 169, respectively. Similarly, at redshift $z = 0$, GADGET-X and GIZMO-SIMBA provide 321 and 302 cluster samples. Further details about our sample of selected clusters and their sub-halos can be found in Table 1 and Table 2. In our analysis, we found the following:

- The cumulative sub-halo mass function shows an overall consistency between MACSJ0416 and MACSJ1206 clusters from M20 and the GIZMO-SIMBA simulation with $R_{2D} < 0.15 R_{200c}$ (Figure 1, left). However, for GADGET-X, agreement between the observation and simulation is only found at a higher sub-halos mass range. The discrepancy at the low-mass end is attributed to a stronger resolution dependence in the baryon model of GADGET-X. The 2D vs 3D comparison of the sub-halo mass function (as shown in Figure 1) highlights the substantial impact of projection effects, revealing a two-fold increase in sub-halo numbers in 2D compared to 3D.
- The redshift evolution study of cumulative sub-halos mass function reveals that while the median halo mass increases with decreasing redshift, the number of sub-halos within massive clusters decreases toward the present time. The analysis of the normalised sub-halo mass function shows a clear redshift evolution, where a greater number of sub-halos are expected to be observed at earlier times when they are less concentrated within their host halos. The sub-halo mass function for both GADGET-X and GIZMO-SIMBA at $z = 0$ is lower (fewer sub-halos) compared to $z = 0.394$, indicating a decrease in the number of sub-halos within host halos over time (Figure 2).
- Both GADGET-X and GIZMO-SIMBA simulations consistently show lower circular V_{circ} for sub-halos compared to the fitting line

obtained from observations when following the distance constraint $R_{2D} < 0.15 R_{200c}$. However, GIZMO-SIMBA exhibits slightly higher V_{circ} values than GADGET-X. Furthermore, GIZMO-SIMBA shows a weak redshift evolution with higher V_{circ} at $z = 0.394$ compared to $z = 0$, unlike GADGET-X.

- The $M_{\text{sub}} - V_{\text{circ}}$ relationship for sub-halos with masses $M_{\text{sub}} < 10^{11} h^{-1} M_{\odot}$ shows a noticeable difference between observations and simulations. This discrepancy is particularly relevant in the context of GGSL. On the other hand, when considering massive sub-halos with $M_{\text{sub}} > 4 \times 10^{11} h^{-1} M_{\odot}$, where simulations are a little closer to observed fitting relation, albeit not in perfect agreement, the significance of the discrepancy decreases due to the limited number of observed sub-halos within this mass range. Therefore, in this range of sub-halo masses, the observed fitting relation of M20 is extrapolated. The contrasting results obtained from the GADGET-X and GIZMO-SIMBA simulations indicate potential to address this issue by fine-tuning the baryon models used in the simulations. However, as shown by Meneghetti et al. (2022), this fine-tuning is difficult to achieve on the mass scales relevant for GGSL without creating inconsistencies with observations at higher masses. For example, simulations with high star formation efficiency and/or lower energy feedback from AGNs produce an excess of galaxies with masses $\gtrsim 10^{12} M_{\odot}$ compared to observations. Meneghetti et al. (in prep.) noted that the GIZMO-SIMBA simulations exhibit this problem.
- The Spearman correlation analysis between sub-halo/galaxy properties and the residual ds reveals that both simulations agree that there is a correlation or anti-correlation between ds and various sub-halo/galaxy properties (Figure 5). The significant sub-halo properties that notably impact the residual ds are the galaxy stellar age,

distance from the cluster's centre (R_{3D}), sub-halo half mass radius, and baryon fraction. The Spearman correlation value indicates that the sub-halo half mass radius and being further away from the cluster centre is associated with a more significant deviation from the observed $M_{\text{sub}} - V_{\text{circ}}$ relation. On the other hand, older galaxy stellar age (formed earlier) and higher sub-halo baryonic mass fraction tend to bring the simulated sub-halo V_{circ} closer to the observed relation.

- Upon comparing the sub-halo properties of GADGET-X and GIZMO-SIMBA, it is evident that GADGET-X exhibits slightly higher baryonic content in its simulated clusters' sub-halos (Figure 6). Additionally, the distribution of galaxy ages is highly comparable between GADGET-X and GIZMO-SIMBA, with a slightly higher proportion of young galaxies in GADGET-X (Figure 6). From the Spearman correlation analysis of sub-halo properties, we would anticipate that GADGET-X will be closer to the observation fitting line compared to GIZMO-SIMBA; however, we observed the opposite. Specifically, the size and concentration of sub-halos/galaxies are identified as crucial factors that contribute to the differences in the $M_{\text{sub}} - V_{\text{circ}}$ relation, with GIZMO-SIMBA having smaller sizes and higher concentrations compared to GADGET-X. The differences in sub-halo properties imply that creating even more compact sub-halos/galaxies, maybe through earlier galaxy formation, may result in improved model-observational data alignment.

- Investigation of global host halo properties in relation to the $M_{\text{sub}} - V_{\text{circ}}$ relationship reveals that relaxed halos exhibit the strongest alignment with observations (negative correlation with COM offset and \overline{ds}). A modest negative correlation between spin parameters and \overline{ds} indicates a tendency for slow-rotating halos to be closer to the observed fitting line, albeit with a weak correlation. Additionally, positive correlation is observed between \overline{ds} and the halo baryon fraction, suggesting a connection to the baryon fraction of sub-halos (Figure 7).

In conclusion, our analysis of galaxy clusters simulated using both GADGET-X and GIZMO-SIMBA in the THE THREE HUNDRED project reveals a discrepancy when comparing them to observations of M20. Our findings suggest that some contemporary simulations struggle to faithfully replicate the observed abundance and compactness of sub-halos. This disparity may arise from limitations in baryonic modeling, systematic challenges within our simulation approaches, uncertainties in observational data and their modeling, or potentially, limitations inherent to the Λ CDM framework.

It is necessary to note here that the comparison done in this paper is based on the AHF halo catalogue instead of SUBFIND in previous studies. We refer to Onions et al. (2012) and Castro et al. (2023) for detailed comparisons between different sub-halo finders and discussions. Both AHF and SUBFIND have unbinding processes to remove the particles that are not gravitationally bound to the sub-halo. This is inconsistent with the sub-halo mass measured in observation apart from the projection effect. Nevertheless, using the observation-like sub-halo mass, will only increase the discrepancy between simulation and observation for both will increase the sub-halo mass and shift the simulated $M_{\text{sub}} - V_{\text{circ}}$ towards the right side, i.e. away from the observed fitting line.

ACKNOWLEDGEMENTS

The authors would like to express their sincere gratitude to Frazer Pearce and Elena Rasia for the insightful discussion and helpful comments, which significantly improved the analytical aspect of this work. WC is supported by the STFC AGP Grant ST/V000594/1 and the Atracción de Talento Contract no. 2020-T1/TIC-19882 granted

by the Comunidad de Madrid in Spain. He also thanks the Ministerio de Ciencia e Innovación (Spain) for financial support under Project grant PID2021-122603NB-C21 and ERC: HORIZON-TMA-MSCA-SE for supporting the LACEGAL-III project with grant number 101086388. Carlo Giocoli thanks the support from INAF theory Grant 2022: Illuminating Dark Matter using Weak Lensing by Cluster Satellites.

The high-resolution simulations were performed at the MareNostrum Supercomputer of the BSC-CNS through The Red Española de Supercomputación grants (AECT-2022-3-0027, AECT-2023-1-0013), and at the DIaL – DiRAC machines at the University of Leicester through the RAC15 grant: Seedcorn/ACTP317

DATA AVAILABILITY

The data underlying this article will be shared on reasonable request to the corresponding author. The simulation data is provided by the300 collaboration which can also be accessed upon request on their website.

REFERENCES

- Anglés-Alcázar D., Özel F., Davé R., Katz N., Kollmeier J. A., Oppenheimer B. D., 2015, *The Astrophysical Journal*, 800, 127
- Anglés-Alcázar D., Davé R., Faucher-Giguère C.-A., Özel F., Hopkins P. F., 2017a, *Monthly Notices of the Royal Astronomical Society*, 464, 2840
- Anglés-Alcázar D., Faucher-Giguère C.-A., Kereš D., Hopkins P. F., Quataert E., Murray N., 2017b, *Monthly Notices of the Royal Astronomical Society*, 470, 4698
- Ansarifard S., et al., 2020, *Astronomy & Astrophysics*, 634, A113
- Armitage T. J., Kay S. T., Barnes D. J., Bahé Y. M., Dalla Vecchia C., 2019, *Monthly Notices of the Royal Astronomical Society*, 482, 3308
- Bahé Y. M., 2021, *Monthly Notices of the Royal Astronomical Society*, 505, 1458
- Bahé Y. M., et al., 2019, *Monthly Notices of the Royal Astronomical Society*, 485, 2287
- Beck A. M., et al., 2016, *Monthly Notices of the Royal Astronomical Society*, 455, 2110
- Bergamini P., et al., 2019, *Astronomy & Astrophysics*, 631, A130
- Bhattacharyya S., Adhikari S., Banerjee A., More S., Kumar A., Nadler E. O., Chatterjee S., 2022, *The Astrophysical Journal*, 932, 30
- Bondi H., 1952, *Monthly Notices of the Royal Astronomical Society*, 112, 195
- Bullock J. S., Kolatt T. S., Sigad Y., Somerville R. S., Kravtsov A. V., Klypin A. A., Primack J. R., Dekel A., 2001, *Monthly Notices of the Royal Astronomical Society*, 321, 559
- Castro T., et al., 2023, *Astronomy & Astrophysics*, 671, A100
- Chabrier G., 2003, *Publications of the Astronomical Society of the Pacific*, 115, 763
- Choi E., Ostriker J. P., Naab T., Johansson P. H., 2012, *The Astrophysical Journal*, 754, 125
- Contreras-Santos A., Knebe A., Cui W., Haggard R., Pearce F., Gray M., De Petris M., Yepes G., 2023, *MNRAS*, 522, 1270
- Cui W., 2022, in *mm Universe @ NIKA2 - Observing the mm Universe with the NIKA2 Camera*. p. 00011 ([arXiv:2111.01889](https://arxiv.org/abs/2111.01889)), doi:10.1051/epjconf/202225700011
- Cui W., Power C., Borgani S., Knebe A., Lewis G. F., Murante G., Poole G. B., 2017, *MNRAS*, 464, 2502
- Cui W., et al., 2018, *Monthly Notices of the Royal Astronomical Society*, 480, 2898
- Cui W., et al., 2022, *Monthly Notices of the Royal Astronomical Society*, 514, 977
- Davé R., Thompson R., Hopkins P. F., 2016, *Monthly Notices of the Royal Astronomical Society*, 462, 3265

- Davé R., Anglés-Alcázar D., Narayanan D., Li Q., Rafieferantsoa M. H., Appleby S., 2019, *Monthly Notices of the Royal Astronomical Society*, 486, 2827
- De Luca F., De Petris M., Yepes G., Cui W., Knebe A., Rasia E., 2021, *MNRAS*, 504, 5383
- Despali G., Vegetti S., 2017, *Monthly Notices of the Royal Astronomical Society*, 469, 1997
- Despali G., Lovell M., Vegetti S., Crain R. A., Oppenheimer B. D., 2020, *Monthly Notices of the Royal Astronomical Society*, 491, 1295
- Ferragamo A., et al., 2023, *MNRAS*, 520, 4000
- Finkelstein S. L., et al., 2022, *ApJ*, 940, L55
- Gao L., White S. D., Jenkins A., Stoehr F., Springel V., 2004, *Monthly Notices of the Royal Astronomical Society*, 355, 819
- Gao L., Frenk C., Boylan-Kolchin M., Jenkins A., Springel V., White S., 2011, *Monthly Notices of the Royal Astronomical Society*, 410, 2309
- Giocoli C., Moreno J., Sheth R. K., Tormen G., 2007, *Monthly Notices of the Royal Astronomical Society*, 376, 977
- Giocoli C., Tormen G., Van Den Bosch F. C., 2008, *Monthly Notices of the Royal Astronomical Society*, 386, 2135
- Giocoli C., Tormen G., Sheth R. K., van den Bosch F. C., 2010, *Monthly Notices of the Royal Astronomical Society*, 404, 502
- Green S. B., van den Bosch F. C., Jiang F., 2021, *Monthly Notices of the Royal Astronomical Society*, 503, 4075
- Haardt F., Madau P., 1995, arXiv preprint astro-ph/9509093
- Haardt F., Madau P., 2012, *The Astrophysical Journal*, 746, 125
- Haggard R., Gray M. E., Pearce F. R., Knebe A., Cui W., Mostoghiu R., Yepes G., 2020b, *MNRAS*, 492, 6074
- Haggard R., Gray M. E., Pearce F. R., Knebe A., Cui W., Mostoghiu R., Yepes G., 2020a, *Monthly Notices of the Royal Astronomical Society*, 492, 6074
- Haggard R., Kuchner U., Gray M. E., Pearce F. R., Knebe A., Yepes G., Cui W., 2023, *MNRAS*, 518, 1316
- Hopkins P. F., 2015, *Monthly Notices of the Royal Astronomical Society*, 450, 53
- Joshi G. D., Parker L. C., Wadsley J., Keller B. W., 2019, *Monthly Notices of the Royal Astronomical Society*, 483, 235
- Klypin A., Yepes G., Gottlöber S., Prada F., Hess S., 2016, *Monthly Notices of the Royal Astronomical Society*, 457, 4340
- Knollmann S. R., Knebe A., 2009, *The Astrophysical Journal Supplement Series*, 182, 608
- Li Q., et al., 2020, *MNRAS*, 495, 2930
- Li Q., et al., 2023, *MNRAS*, 523, 1228
- Lotz J. M., et al., 2017, *ApJ*, 837, 97
- Marinacci F., et al., 2018, *Monthly Notices of the Royal Astronomical Society*, 480, 5113
- Meneghetti M., et al., 2020, *Science*, 369, 1347
- Meneghetti M., et al., 2022, *A&A*, 668, A188
- Mostoghiu R., Knebe A., Cui W., Pearce F. R., Yepes G., Power C., Dave R., Arth A., 2019, *MNRAS*, 483, 3390
- Murante G., Monaco P., Giovali M., Borgani S., Diaferio A., 2010, *Monthly Notices of the Royal Astronomical Society*, 405, 1491
- Naidu R. P., et al., 2022, *ApJ*, 940, L14
- Naiman J. P., et al., 2018, *Monthly Notices of the Royal Astronomical Society*, 477, 1206
- Navarro J. F., 1996, in *Symposium-international astronomical union*. pp 255–258
- Nelson D., et al., 2019, *Computational Astrophysics and Cosmology*, 6, 1
- Onions J., et al., 2012, *MNRAS*, 423, 1200
- Peebles P., 1969, *Astrophysical Journal*, vol. 155, p. 393, 155, 393
- Pillepich A., et al., 2018, *Monthly Notices of the Royal Astronomical Society*, 475, 648
- Planck Collaboration et al., 2016, *A&A*, 594, A13
- Planelles S., Borgani S., Fabjan D., Killedear M., Murante G., Granato G. L., Ragone-Figueroa C., Dolag K., 2014, *Monthly Notices of the Royal Astronomical Society*, 438, 195
- Planelles S., et al., 2017, *Monthly Notices of the Royal Astronomical Society*, 467, 3827
- Postman M., et al., 2012, *ApJS*, 199, 25
- Power C., Navarro J. F., Jenkins A., Frenk C. S., White S. D., Springel V., Stadel J., Quinn T., 2003, *Monthly Notices of the Royal Astronomical Society*, 338, 14
- Prada F., Klypin A. A., Cuesta A. J., Betancort-Rijo J. E., Primack J., 2012, *Monthly Notices of the Royal Astronomical Society*, 423, 3018
- Ragagnin A., Dolag K., Moscardini L., Biviano A., D’Onofrio M., 2019, *Monthly Notices of the Royal Astronomical Society*, 486, 4001
- Ragagnin A., et al., 2022, *Astronomy & Astrophysics*, 665, A16
- Ragone-Figueroa C., Granato G. L., Ferraro M. E., Murante G., Biffi V., Borgani S., Planelles S., Rasia E., 2018, *Monthly Notices of the Royal Astronomical Society*, 479, 1125
- Rahmati A., Pawlik A. H., Raičević M., Schaye J., 2013, *Monthly Notices of the Royal Astronomical Society*, 430, 2427
- Rasia E., et al., 2015, *The Astrophysical Journal Letters*, 813, L17
- Robertson A., 2021, *Monthly Notices of the Royal Astronomical Society: Letters*, 504, L7
- Sayers J., Mantz A. B., Rasia E., Allen S. W., Cui W., Golwala S. R., Morris R. G., Wan J. T., 2023, *ApJ*, 944, 221
- Smith B. D., et al., 2017, *Monthly Notices of the Royal Astronomical Society*, 466, 2217
- Springel V., 2005, *Monthly notices of the royal astronomical society*, 364, 1105
- Springel V., Hernquist L., 2003, *Monthly Notices of the Royal Astronomical Society*, 339, 289
- Springel V., White S. D., Tormen G., Kauffmann G., 2001, *Monthly Notices of the Royal Astronomical Society*, 328, 726
- Springel V., et al., 2018, *Monthly Notices of the Royal Astronomical Society*, 475, 676
- Steinborn L. K., Dolag K., Hirschmann M., Prieto M. A., Remus R.-S., 2015, *Monthly Notices of the Royal Astronomical Society*, 448, 1504
- Tormen G., 1998, *Monthly Notices of the Royal Astronomical Society*, 297, 648
- Tornatore L., Borgani S., Dolag K., Matteucci F., 2007, *Monthly Notices of the Royal Astronomical Society*, 382, 1050
- White S. D., Frenk C. S., 1991, *Astrophysical Journal*, Part 1 (ISSN 0004-637X), vol. 379, Sept. 20, 1991, p. 52-79. Research supported by NASA, NSF, and SERC., 379, 52
- Wiersma R. P., Schaye J., Smith B. D., 2009, *Monthly Notices of the Royal Astronomical Society*, 393, 99
- Yang D., Yu H.-B., 2021, *Physical Review D*, 104, 103031
- Zhang B., Cui W., Wang Y., Dave R., De Petris M., 2022, *MNRAS*, 516, 26
- de Andres D., et al., 2022, *Nature Astronomy*, 6, 1325
- van den Bosch F. C., Ogiya G., Hahn O., Burkert A., 2018, *Monthly Notices of the Royal Astronomical Society*, 474, 3043

This paper has been typeset from a \LaTeX file prepared by the author.